Earth and Planetary Science Letters 420 (2015) 174–186

Contents lists available at ScienceDirect

Earth and Planetary Science Letters

www.elsevier.com/locate/epsl

Upper mantle structure beneath southern African cratons from seismic finite-frequency P- and S-body wave tomography

M. Youssof[a,*], H. Thybo[a], I.M. Artemieva[a], A. Levander[b]

[a] *Geology Section, Department of Geosciences and Natural Resource Management (IGN), University of Copenhagen, DK-1350 Copenhagen-K, Denmark*
[b] *Department of Earth Science, Rice University, Houston, TX 77005-1892, USA*

ARTICLE INFO

Article history:
Received 17 March 2014
Received in revised form 20 January 2015
Accepted 25 January 2015
Available online 14 April 2015
Editor: P. Shearer

Keywords:
finite-frequency sensitivity kernels
body wave teleseismic tomography
cratonic lithosphere
Kaapvaal Craton
Bushveld Complex

ABSTRACT

We present a 3D high-resolution seismic model of the southern African cratonic region from teleseismic tomographic inversion of the P- and S-body wave dataset recorded by the Southern African Seismic Experiment (SASE). Utilizing 3D sensitivity kernels, we invert traveltime residuals of teleseismic body waves to calculate velocity anomalies in the upper mantle down to a 700 km depth with respect to the ak135 reference model. Various resolution tests allow evaluation of the extent of smearing effects and help defining the optimum inversion parameters (i.e., damping and smoothness) for regularizing the inversion calculations.

The fast lithospheric keels of the Kaapvaal and Zimbabwe cratons reach depths of 300–350 km and 200–250 km, respectively. The paleo-orogenic Limpopo Belt is represented by negative velocity perturbations down to a depth of ∼250 km, implying the presence of chemically fertile material with anomalously low wave speeds. The Bushveld Complex has low velocity down to ∼150 km, which is attributed to chemical modification of the cratonic mantle. In the present model, the finite-frequency sensitivity kernels allow to resolve relatively small-scale anomalies, such as the Colesberg Magnetic Lineament in the suture zone between the eastern and western blocks of the Kaapvaal Craton, and a small northern block of the Kaapvaal Craton, located between the Limpopo Belt and the Bushveld Complex.

1. Introduction

Jordan (1975, 1978, 1988) introduced the term tectosphere to describe the architecture of cratonic roots as thermally conductive media with gentle geothermal gradients, unique composition of the lithospheric mantle, and seismologically fast keels that may extend down to the transition zone. His isopycnic hypothesis resolves the paradox of how the cold cratonic upper mantle may be in isostatic balance with warmer oceanic plates: the negative thermal buoyancy (densification associated with thermal contraction) of cold cratonic lithosphere is compensated by its intrinsic chemical buoyancy imparted by the low densities of melt-depleted peridotites as compared to fertile oceanic peridotites.

Earlier studies of cratons emphasize that the highly depleted Archean lithosphere is always characterized by inherently faster seismic wavespeed than younger Proterozoic lithosphere (e.g., Jordan, 1975, 1978, 1988; Lebedev et al., 2009; Darbyshire et al., 2012). Other studies suggest that there is a correlation between inferred lithospheric age and seismic characteristics (e.g., Fishwick et al., 2005). The depth extent of the cratonic keels and their layering are still controversial issues (Rudnick et al., 1998; Kopylova and Russell, 2000; Artemieva and Mooney, 2001; Artemieva, 2009, 2011; Gung et al., 2003; Lehtonen et al., 2004; Fischer et al., 2010; Yuan and Romanowicz, 2010). The nature of keel development is a complex question which is under debate, specifically concerning the extent to which tectonics and thermochemical processes after formation of the tectosphere nucleus, have contributed towards vertically stratified lithospheric mantle (e.g., Lehtonen et al., 2004; Artemieva, 2011; Kopylova and McCammon, 2003). Many studies of controlled source seismology (Perchuć and Thybo, 1996; Thybo and Perchuć, 1997; Thybo, 2006), receiver functions (Fischer et al., 2010; Rychert and Shearer, 2009; Abt et al., 2010; Wirth and Long, 2014; Lekić and Fischer, 2013; Cooper and Miller, 2014; Hopper et al., 2014), and tomographic studies (Yuan and Romanowicz, 2010), yield evidences for either a single or multiple mid lithospheric discontinuities. Given that the mid lithospheric discontinuity is always observed at ∼100 km depth, it may be explained by thermochemical processes in the depth range where the geotherm approaches the solidus of mantle material containing small amounts of volatiles

---

[*] Corresponding author. Address: Øster Voldgade 10, 1350 Copenhagen, Denmark. Tel.: +45 52639916, +49 17699581102; fax: +45 35322501.
E-mail addresses: ms@ign.ku.dk, soliman@gfz-potsdam.de (M. Youssof).

http://dx.doi.org/10.1016/j.epsl.2015.01.034

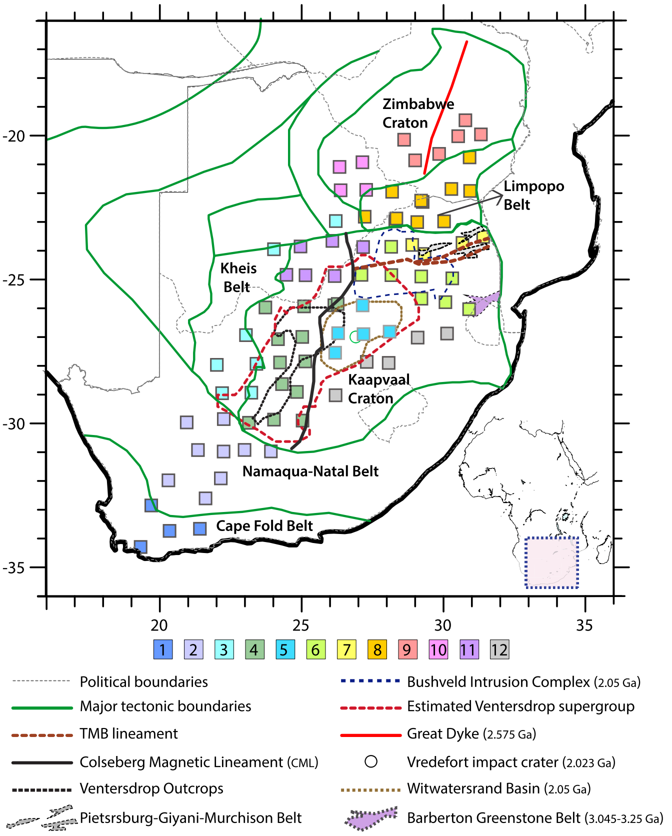

Fig. 1. Station locations in the southern African region showing the 82 stations of the SASE array. Color code for the SASE array corresponds to the numbering of tectonic blocks as follows. 1: Cape Fold Belt, 2: Namaqua–Natal Mobile Belt, 3: Kheis–Okwa Mobile Belt, 4: Western Kaapvaal Craton – Ventersdorp LIP, 5: Central Kaapvaal Craton – Witwatersrand basin, 6: Northern Kaapvaal Craton – Bushveld Igneous Complex, 7: Northern Kaapvaal Craton – Pietersburg/Giyami/Murchison, 8: Limpopo Mobile Belt, 9: Zimbabwe Craton – Tokwe gneiss block, 10: W Zimbabwe craton – Tati Granite–Greenstone, 11: NW Kaapvaal Craton – Late Archean Gaberone Granites,12: Eastern Kaapvaal Craton. (For interpretation of the references to color in this figure legend, the reader is referred to the web version of this article.)

(Thybo and Perchuć, 1997; Thybo, 2006). Furthermore, (Darbyshire et al., 2012) demonstrates that variations in wavespeed occur vertically with fast wavespeed structure in the upper ∼150 km (interpreted as Archean material) lithosphere above younger mantle with lower wavespeed. This model, which builds on earlier studies of the North American Cratons (Darbyshire et al., 2012; Yuan and Romanowicz, 2010), implies that keels can form at different times and in different ways suggesting a two-layered structure in which the lower layer might have been accreted to the base of the existing cratonic lithosphere. Alternatively, the lower part of the cratonic lithospheric mantle (below ca. 150–180 km depth) may have been significantly metasomatised during long-lasting lithosphere-mantle interaction as indicated by the differences in shear-wave speeds corrected for regional temperature variations in the mantle (Artemieva, 2009).

Keel depth beneath the cratons is still poorly understood in general (e.g., Artemieva and Mooney, 2001; Artemieva, 2009; Eaton et al., 2009). To examine the depth extent of cratonic keels, their seismic velocity heterogeneities, and to shed light on the tectosphere evolution, we apply teleseismic tomography for imaging the upper mantle seismic velocity structure beneath the southern African cratonic regions: the Kaapvaal and Zimbabwe cratons separated by the Limpopo Belt, including the adjacent Namaqua–Natal and Cape Fold Belts.

Previous estimates of lithosphere keel thickness in southern Africa by receiver functions and body wave tomography interpretations differ significantly from 140–160 km (Vinnik et al., 2009; Hansen et al., 2009; Zhao et al., 1999) to about 300–370 km (Vinnik et al., 1996; Kumar et al., 2007; Wittlinger and Farra, 2007), or even with a complex fashion by showing a layered events in the region of the base of the tectosphere (Levander et al., 2006), and also differ from results based on surface wave tomography which leads to thickness ranges from 170 to ∼250 (Fischer et al., 2010; Priestley et al., 2006, 2008; Sebai et al., 2006; Li and Burke, 2006; Chevrot and Zhao, 2007; Adams and Nyblade, 2011). The latter values of the lithosphere thickness in the Precambrian regions of southern Africa are supported by thermal modeling (Artemieva and Mooney, 2001). Another study (Sodoudi et al., 2014) reveals the presence of distinct lithospheric layers throughout the stable part of the Kalahari craton and suggests that the lithosphere–asthenosphere boundary (LAB) is extremely deep under the Archean core and tapers out toward the surrounding Paleozoic borders.

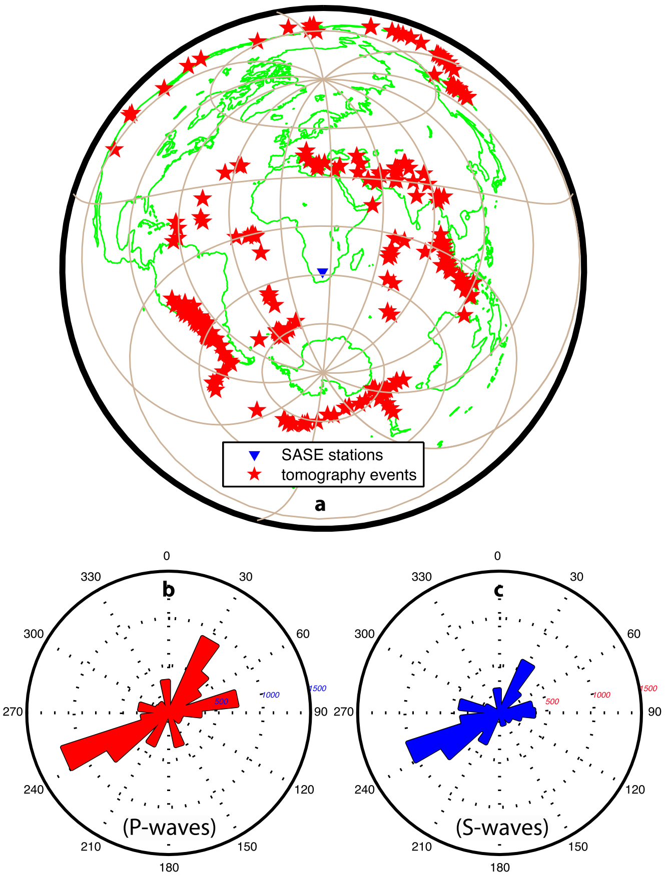

Fig. 2. (a) Event distribution map used in this study, in equidistant projection, centered on the middle of SASE array. The lower insets are rose diagrams which show the backazimuthal coverage of all the arrivals picked of b) P-waves, and c) S-waves. (For interpretation of the references to color in this figure legend, the reader is referred to the web version of this article.)

Our study builds on data from the dense seismic array of the Southern African Seismic Experiment (SASE) in Kalahari (Carlson et al., 1996). The NE–SW elliptical shape-like array covers tectonic provinces of early Archean to Phanerozoic age, with ∼100 km between stations (Fig. 1). The array provides dense ray-path coverage of the upper mantle which leads to high resolution seismic tomography models down to the transition zone. Additionally, the hypocentral distribution of analyzed events provides relatively good azimuthal coverage (Fig. 2).

The number of seismological tools that have been applied in the study region is incomparable with any other cratonic regions on the globe. Geochemical studies of the abundant mantle-derived xenoliths from kimberlites in southern Africa (Boyd, 1987; Finnerty and Boyd, 1987; Boyd et al., 1993; Pearson et al., 1995; Shirey et al., 2001, 2002; Lee, 2006) provide opportunity to complement the interpretation of our seismic imaging by petrologic information.

Using the same SASE dataset and applying classic geometrical-ray (infinite frequency) theory, previous tomographic body and surface wave inversions have provided insight into the upper mantle of the region (Priestley et al., 2006; James et al., 2001; Fouch et al., 2004; Priestley and Tilmann, 2009). In the present study, we analyze body wave residuals using finite-frequency 3D sensitivity kernels (Marquering et al., 1999; Dahlen et al., 2000; Hung et al., 2000; Montelli et al., 2004a, 2004b; de Hoop and van der Hilst, 2005; Bezada et al., 2010; Schmandt and Humphreys, 2010) to reveal the upper mantle *Vp* and *Vs* anomalies. This multi-frequency-based inversion is superior to ray theory for imaging the upper mantle to obtain realistic representation of its seismic complexity, and includes high frequencies to improve the model resolution. Another advantage of this method for enhancing the final model resolution is that the number of observed picked arrivals is increased by the use of multiple frequency bandwidths. To obtain high-quality waveforms, we inspect the consistency of the station and event measurements to exclude bad traces visually. The relative traveltime residuals are inverted for 3D perturbations in velocity structure. The present tomographic models are determined using linear inversion, appropriate for southern Africa where the velocity anomalies expectedly are relatively small (Priestley et al., 2006; James et al., 2001; Fouch et al., 2004; Priestley and Tilmann, 2009). In the inversion and interpretation, we also take into account the difference of the data density between different parts of the study region (i.e., the number of deployed stations and ray coverage). Given that the Kaapvaal Craton is the best-sampled region in the SASE experiment, the tomographic model is most reliable for this part of southern Africa.

2. Residuals of traveltime data

The seismic dataset includes seismic recording with broadband stations at 82 locations in southern Africa for a period of 1–2 yr (about half of the stations at the periphery of the array operated only for one year). 4471 P- and S-wave absolute arrivals have been handpicked. The differences between these picks and the predicted arrival times from ak135 (Kennett et al., 1995) are used as initial input and quality control during the step of cross-correlation. The absolute travel-time anomalies are computed from the first arriving phase (first break). We then retrieve relative arrival times of phases P, PKPdf, S, and SKS via a multi-channel cross-correlation procedure (VanDecar and Crosson, 1990), which considers the mean phase pick time for all stations across the seismograph network for a given earthquake. The phase arrival times relative to an unknown mean time are obtained by finding the maximum of the cross-correlation function between each possible pair of seismograms. Waveforms from the selected events are band-pass filtered at multi-frequency bands and traveltime delays for each event are obtained by cross correlating the filtered seismograms. Odd-looking seismograms are inspected further and outliers are removed, based on a visual event and station inspection criteria, if the quality is low to minimize the first order timing errors.

The absolute residuals δ_{ij}^{a} are calculated by subtracting the predicted arrival times T_{ij}^{p}, according to the ak135 reference model, from the observed traveltimes T_{ij}^{o}

$$\delta_{ij}^{a} = T_{ij}^{o} - T_{ij}^{p} + \delta T_{ij} \tag{1}$$

$$\delta T_{ij} = \sum_{k=1}^{4} \delta T_{jk} \tag{2}$$

where δT_{jk} are the differences between observations from the predicted reference model. $k = 1$–4 represents various timing uncertainties associated with the jth event. Timing shift in Eq. (2) originates from the uncertainty in 1) source location, 2) event time, and velocity variations in the 3) upper and 4) lower mantle. The distinction between the lower and upper mantle anomalies is introduced because individual rays travel along the same raypath in the lower mantle until the rays diverge in the upper mantle beneath the seismic array. By the procedure of cross-correlation, the residuals corresponding to the traveltime variations can be calculated in the upper mantle beneath all stations that recorded the same jth event. This allows removal of the mean from the data to reduce the average residuals.

The starting point of the linearized formulation for the traveltime tomography in our study utilizes the following equation (Dahlen et al., 2000);

$$\delta t_{ij} = \iiint_{\Theta} K(\mathbf{x})\, \delta s_{ij}(\mathbf{x})\, d^{3}\mathbf{x} \tag{3}$$

where δt_{ij} is an observed traveltime residual relative to that predicted by the one-dimensional, radially-symmetric model, ak135, and $K(\mathbf{x})$ is the Fréchet derivative or sensitivity kernel that relates δt_{ij} to perturbations in P- or S-wave slowness δs_{ij} at every point $\mathbf{x}$ throughout the region, Θ, that is being imaged.

For seismic phases relevant to our study, sensitivity kernels from the finite-frequency theory have the so-called "banana-doughnut" characteristics with minimal sensitivity along the geometrical raypaths (Dahlen et al., 2000; Hung et al., 2000). When the lateral length scale of heterogeneity in wave speeds is considerably greater than the diameter of the 3-D kernel or, equivalently, the frequency of the wave approaches infinity, Eq. (3) simply reduces to linearized ray theory (because the geometrical ray theory is only valid if the scale length of the Earth's 3-D heterogeneity is much greater than the seismic wavelength). In this case, the Fréchet derivative essentially approaches zero everywhere except along the geometrical ray, and Eq. (3) reduces to a line integral of δs at each incremental arc length, evaluated along the geometrical raypath that is determined solely by a 1-D reference model. Based on synthetic traveltime residuals, a number of studies have shown that both finite and infinite-frequency inversion procedures produce comparable results in general terms, but images based on the finite-frequency formulation are superior in recovering both amplitude and geometry of anomalies, i.e. provide better resolution of the inverted model (Montelli et al., 2004a, 2004b).

In the current study, we calculate the relative traveltime residuals for the selected 1) P-phases (recorded for epicentral distances in the ranges of 30°–90° and 140°–180°) on the vertical components and 2) S-phases (recorded for epicentral distances in ranges of 30°–90°) on the SH components after rotation of the shear axes to the radial and transverse wave fields. In total, we use 13 414 body wave residuals (7374 and 6040 for P- and S-waves, respectively) which we calculate by cross-correlation of band-pass filtered waveforms in different Gaussian frequency bands (centered at frequencies of 1, 0.5 and 0.3 Hz for P waves and at 0.1, 0.05 and 0.03 Hz for S waves): all bandwidths are the same as the center frequency values. This means that if the center frequency is 1 Hz, the bandwidth will be 1 s as well. The root mean square (RMS) of the P and S residuals is 0.32 s and 1.00 s before inversion (Figs. 3a, 3b).

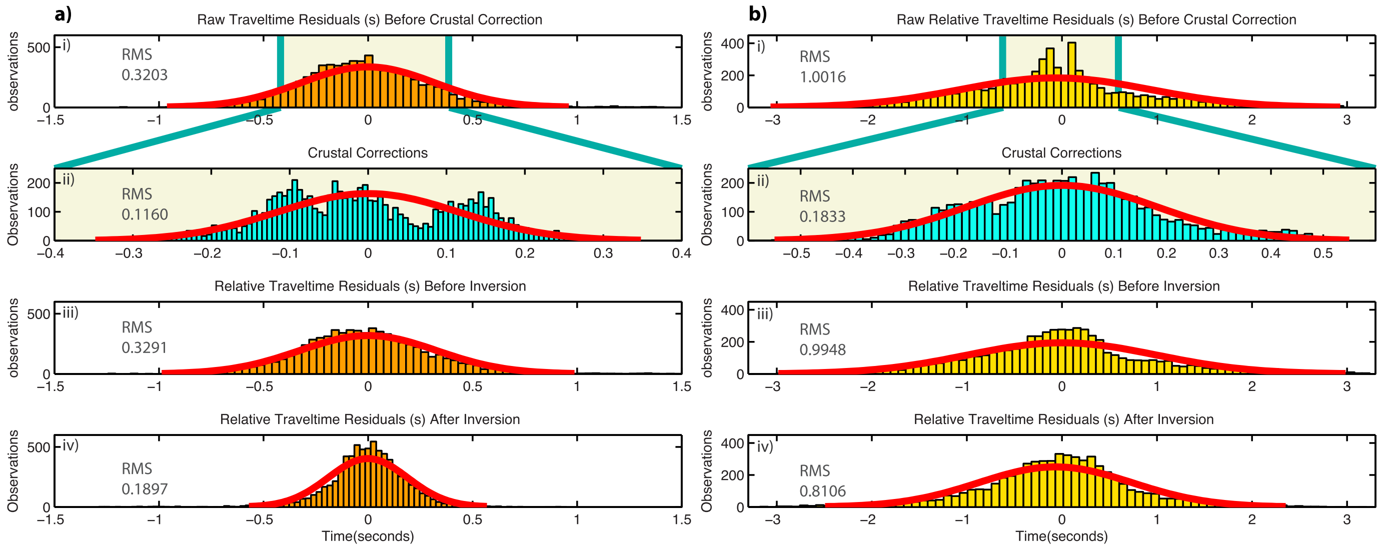

Fig. 3. Histograms for (a) P-wave and (b) S-wave datasets showing the raw measured delaytimes (i), crustal corrections (ii), relative traveltime data before (iii) and after the inversion (iv).

To avoid projection of crustal velocity heterogeneities into the mantle, we apply crustal and elevation corrections to the delay times. Ray theoretical time corrections are calculated based on a crustal model derived from recent results of receiver function calculations for the same array (Youssof et al., 2013). We generally expect that the frequency-dependence of crustal correction times is small for the phases and frequencies in our traveltime dataset (Ritsema et al., 2009). The RMS residual of the corrected traveltime after inversion of the P- and S-waves is 0. 19 s and 0.81 s, respectively, while the crustal corrections have RMS of 0.12 s and 0.18 s (Fig. 3). Interpretation of the data indicates that there is a correlation between the crustal structure and integrated travel-time residuals. This may indicate that inversion-based station terms can be used to correct for crustal structure. We have to take into consideration that the station terms effectively can reduce the magnitude of travel-time residuals and therefore would lead to underestimation of mantle heterogeneity. Smaller variance reduction was achieved for S-wave data than for P-wave data which probably reflects a larger component of measurement error in the S-wave than the P-wave dataset.

3. Tomographic finite-frequency inversion

Traveltimes are sensitive to seismic velocity variations within a volume surrounding the geometrical raypath. Seismic waves with different frequency content have different Fresnel zone widths and sample different volumes of the medium around the geometrical raypath. Therefore, finite-frequency 3D sensitivity kernels (the Born kernel formulation of Dahlen et al., 2000) are preferred as link between traveltime residuals and perturbations of model parameters. In this study, we choose to calculate the sensitivity of the first Fresnel zone (R_{F1}) using an approximate formulation for the finite-frequency kernels (Schmandt and Humphreys, 2010). R_{F1} is measured as a function of epicentral distance (Δ) along the raypath (D_R) with computations at 3° increments of distance. This step is repeated for all selected frequency bands. To estimate R_{F1} for all rays, we interpolate between the different R_{F1} radii. Therefore, the relative distribution of sensitivity within R_{F1} is approximated as

$$K(R_N) = A\sin\left(\pi\left[\frac{R_N}{R_{F1}(D_R,\omega,\Delta)}\right]^2\right) \tag{4}$$

where A is a scaling constant, ω is the frequency and R_N is the ray-normal distance within any ray-normal plane. A is determined by assuming that the integrated value of the full Born kernel in the volume around the ray is equal to the integrated value of ray theoretical sensitivity along the ray length L (Schmandt and Humphreys, 2010):

$$\int_V K(x)dV = \int_L \left[\vartheta(D_R)\right]^{-1} dL \tag{5}$$

where $K(x)$ is the 3D Born sensitivity kernel and $\vartheta(D_R)$ is the reference velocity as a function of position along the ray. We use Eqs. (4) and (5) to approximate sensitivity within the volume of R_{F1} as

$$\begin{aligned} K_{F1}(R_N, D_R, \omega, \Delta) &= \left(\frac{\int_L [\vartheta(D_R)]^{-1} dL}{\int_{V_{F1}} \sin[\pi(\frac{R_N}{R_{F1}(D_R,\omega,\Delta)})^2] dV_{F1}}\right) \\ &\quad \times \sin\left(\pi\left[\frac{R_N}{R_{F1}(D_R,\omega,\Delta)}\right]^2\right) \end{aligned} \tag{6}$$

where V_{F1} represents the entire volume of R_{F1} around the ray length L.

For model regularization, we apply ray normal smoothing to the sensitivity kernels to address ray location uncertainty. The applied smoothing width increases with raypath distance from the station from 2 km at the Moho to 10 km at a distance of 700 km along the raypath. The ak135 1-D velocity model is used as a reference model both for calculation of the raypaths and sensitivity kernels. Model parameterization is designed by nodes at the vertices of an irregular, rectangular 3D mesh, which consists of a total of 48 450 and 44 849 nodes for P- and S-wave datasets, respectively (Table 1). Vertically 25 nodes have variable spacing from 14 to 35 km between the model surface and 100 km depth, from where they occur at 25 km interval down to 400 km depth and at 50 km interval down to 700 km depth. Horizontal node spacing is smallest (35 km) beneath the array center and gradually increases to 45 km at the edges of the model where there are few crossing rays. This gradual coarsening of node spacing parameterization is introduced in order to match the growing width of R_{F1} and decreasing resolution. The model domain extends from 1 km

Table 1
Quantitative characters of the P- and S-wave traveltime datasets and model parameterization.

Data		P-wave	S-wave
Epicentral distance ranges (°)		30°–90° and 140°–180°	30°–90°
Central frequencies (Hz)		1, 0.5, 0.3	0.1, 0.05, 0.03
RMS of P and S residuals (s)	Raw residuals	0.33	0.99
	Corrected residuals	0.19	0.81
	Crustal correction	0.12	0.18
	Station term	0.04	0.04
	Event term	0.05	0.29
Model parameterization	(Number of nodes)	48 450 nodes; 51 (latitudinal) by 38 (longitudinal), in 25 layers	44 849 nodes; 51 (latitudinal) by 38 (longitudinal), in 23 layers

to 700 km depth but resolution is low above 36 km depth as a result of near vertical raypaths in the crust and the clustering of rays at station locations. Corrections for crustal thickness and velocity variations at each station have already been applied to the traveltimes. We apply a station damping to keep the station terms from absorbing mantle structure. The RMS residual of the station terms is 0.04 s for both P and S. Event terms are 0.047 s for P and 0.29 s for S, which represents the correction of the mean arrival time for the set of stations that recorded each of the events.

A combination of smoothing (gradient damping) and norm damping operators is useful to regularize the inverse problem. The smoothing operator is depth-dependent and the weight of the constraint is greatest in the plane normal to the mean raypath orientation. We use this operator to produce smooth velocity variations, both laterally and radially. Norm damping finds the minimum structure solution that satisfies the traveltime data and reduces perturbations that are weakly constrained by the data. This tends to minimize the amplitude of the velocity perturbations. We have selected the optimized norm damping that reasonably recovers the amplitude of well-sampled anomalies while eliminating strong perturbations in poorly sampled cases. Both damping parameters are chosen, as is common practice, in a subjective manner, inspecting a trade-off graph of the misfit of the solution against complexity of the model (Fig. S5).

The iterative LSQR method used to solve the inverse problem seeks a solution (m) which minimizes the least-squares misfit (E) (Paige and Saunders, 1982). This optimal solution of the regularized inversion can be found to minimize the cost function

$$E = \|Gm - d\|^2 + K_1\|Lm\|^2 + K_2\|m\|^2 \tag{7}$$

where G is the matrix of the partial derivatives that relates the corrected traveltime residuals (d) to perturbations in model parameters of vector m. The L matrix represents the spatially varying smoothing constraint while K_1 and K_2 are the relative weights of the smoothing and damping terms, respectively. The values of K_1 and K_2 for the P- and S-wave datasets are proportional to the magnitudes of the P and S data vectors. The damping parameters can be determined on the basis of a trade-off curve between model norm and variance reduction (Eberhart-Philips, 1986). This trade-off with varying damping coefficient K_2 is represented by the L-curve which can be obtained for each smoothing factor K_1 by adding the smoothness constraint (Fig. S5). Varying the model box volume or changing the damping progressively through depth within the same inversion provides realistic insight into the imaged anomalies ("squeezing tests"; Lerner-Lam and Jordan, 1987). We ran both suites of tests with a fine interval of 1 unit at all the values of damping and smoothing (where K_1 and K_2 both range from 1 to 50, Fig. S5). Based on this criterion, we select the optimum $K_1 = 16$ and $K_2 = 25$ factors separately, to be used for the *Vp*- and *Vs*-datasets inversion.

4. Resolution assessment

We investigate the resolution of velocity anomaly recovery through different kinds of synthetic tests that demonstrate expected model resolution, under the assumption of an isotropic elastic mantle, accurate ray locations, and banana doughnut-like traveltime sensitivity. In the first type of resolution tests, the synthetic velocity structure consists of a group of checkerboard layers, with each anomalous volume consisting of 5 nodes at the vertices from 1.5° to 2° cube (block size increases slightly from the model surface center in all directions with node spacing). The input structure is reasonably well recovered by the final model, but the amplitudes are only 50% or less of the model anomaly (Fig. 4, Fig. S4). We observe smearing and amplitude loss of the input structure caused by the near-vertical propagation of teleseismic rays and the preference for minimum energy structure in the inversion algorithm as well as the uneven distribution of back-azimuths. The peak amplitude recovery is slightly better in the P-wave test than in the S-wave test. We attribute this to the shorter wavelengths and larger number of teleseismic P-wave arrivals. Larger input anomalies tend to reduce the difference between the P and S recovery model. For the current study, input anomalies of 1.0% for P-wave and 2.5% for S-wave perturbations are the optimum, as we do not expect larger anomalies in mantle structures. Checkerboard resolution tests show a reasonable model recovery for Vp and Vs anomalies imaged over block dimensions of $\sim 1.5° \times 1.5°$ laterally and with ~150 km in thickness.

In order to interpret the small-scale features in the present tomographic model, we apply two different resolution tests: squeezing tests and model-driven tests to get indication of the depth extent of the cratons. The checkerboard test indicates that the horizontal resolution is better than 100 km in the upper 200–300 km (best for the P-wave model). The interval of 200–500 km is characterized by strong NW–SE directed smoothing due to the low density of back-azimuthal rays coverage in this direction (Fig. 2) and surprisingly the test indicates good recovery below 500 km. The classical checkers define systematic/periodic changes of velocity that have the tendency to be recovered by the linear inversion, so, checkerboard test may not give full insight into the actual resolution (Allen and Tromp, 2005; Leveque and Masson, 1999; Alinaghi et al., 2007; Foulger et al., 2013). Finite-frequency kernels suffer the same limitation in depth resolution for regional teleseismic studies as ray theory and therefore squeezing tests are used here to determine if a velocity anomaly could be isolated within just one part of the kernel volume while satisfying the dataset (Alinaghi et al., 2007).

To isolate the depth extent of anomalies, we perform the so-called squeezing tests (Figs. S6, S7). These tests include two suites: 1) to apply the optimum K_1 and K_2, equally through the entire model, with model depth being selected at 200, 300, 500, 700 and to 1000 km and 2) for the selected 700 km deep model, to increase the damping parameter K_2 in the deeper layers progressively and examine the RMS misfit and the imaged structure

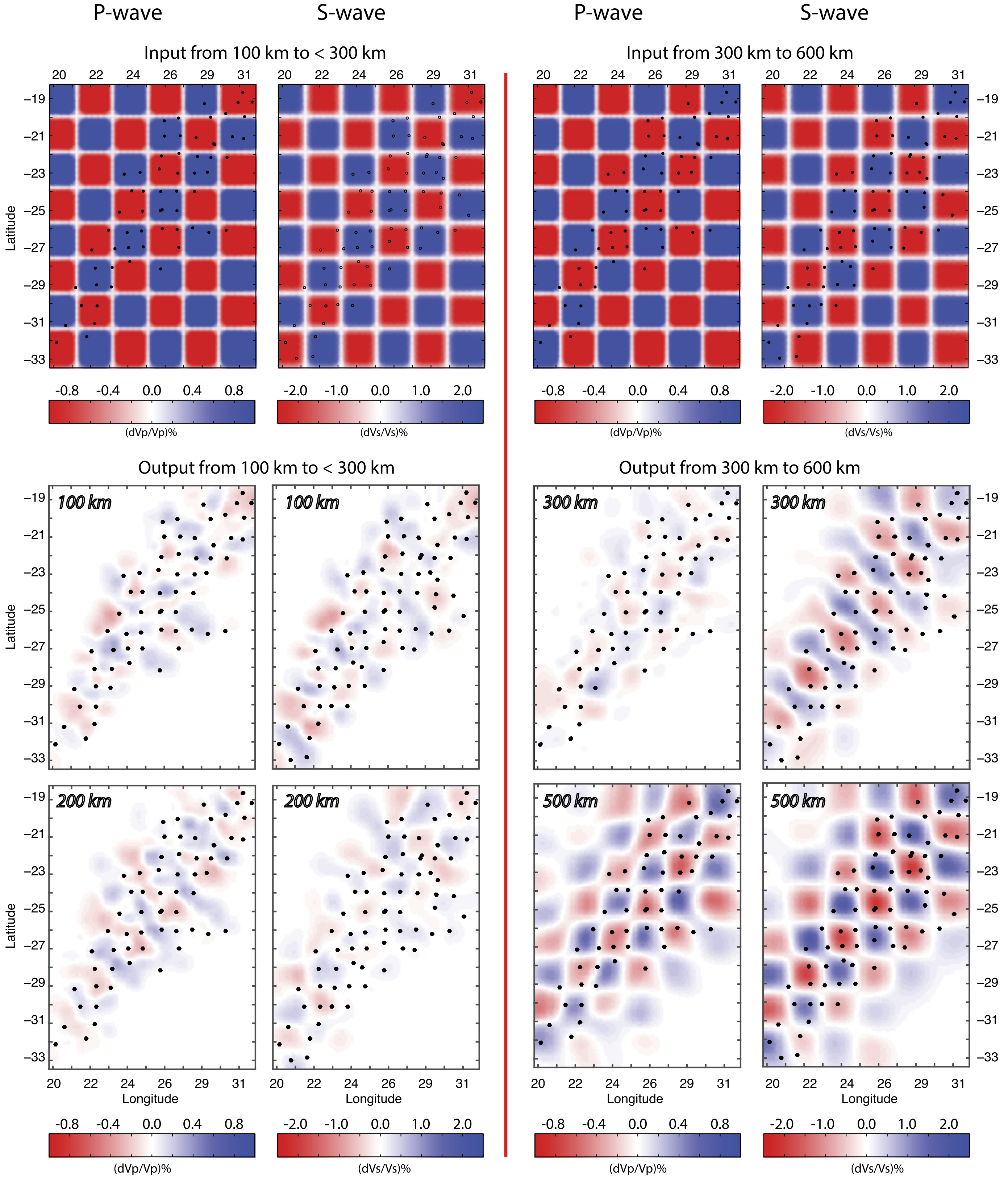

Fig. 4. Finite-frequency checkerboard resolution tests for P- and S-wave dataset. The upper panels show the input model. Synthetic output is presented in the form of 4 different horizontal slices. The effects of vertical streaking is observed at shallow depth. All images have been plotted with the same color-scale so that the degree of pattern and amplitude recovery are comparable. (For interpretation of the references to color in this figure legend, the reader is referred to the web version of this article.)

Table 2
Results of the suites of squeezing tests. Test-1: applying the same factors of $K_2 = 16$ and $K_1 = 25$ through the whole model but with changing model size. Test-2: applying different values of K_1 and K_2 below 400 km depth, through the same selected model of 700 km depth, which has been selected as an optimum model.

Test-1		
Model maximum depth (H, km)	Fixed $K_2 = 16$	
	RMS of inverted data (s)	Variance reduction (%)
1000	0.18	70.73
700	0.19	66.78
500	0.20	63.06
300	0.21	57.91
200	0.22	53.14

Test-2		
K_2 changes below 400 km to	Fixed $H = 700$ km	
	RMS misfit	Variance reduction (%)
32	0.22	57.04
64	0.26	39.15
96	0.28	26.32

(Table 2). For test-1, the RMS misfit decreases and the variance reduction increases with increasing thickness of the model box. For test-2, K_2 values are changed from 400 km depth to the bottom of the model, where K_2 is increased to 2, 4, and 6 times the optimum K_2, which is applied in the upper 400 km and chosen by the trade-off analysis. RMS misfit increases and the resultant variance reduction decreases significantly through the increase of K_2 (Table 2 and supplementary Table S1). Vertical slices through the squeezed final models for both test-1 and test-2 show that the lateral distribution of structures remains unaffected by the depth extent of the model, and that deep structures remain present for strong damping (Figs. S6, S7). This indicates that the anomalies in the whole upper-mantle are required by the data.

To test the effect of vertical smearing on the imaged velocity anomalies, a third type of resolution tests is performed (structure-driven test (Fig. 5)), where synthetic anomalies in the form of simplified blocks simulate the imaged structures in the tomographic model (Alinaghi et al., 2007). This test may add constraints to the depth extent of the imaged anomalies. Two synthetic inputs are used for this test. The first model (test-a) replicates the Kaapvaal Craton body (positive anomaly) surrounded by the southern mobile belts, and divided by the Bushveld Complex (negative anomaly) where all of the anomalies extend to 300 km depth. The mantle below 300 km depth is neutral with velocity as in the ak135 reference model (Fig. 5a). The second test (test-b) has the same structure as test-a to 300 km depth with negative anomaly everywhere below a depth of 300 km (Fig. 5b). For both tests, all structures (and even the northern small block of the Kaapvaal Craton) are returned in the output model and, in the best case, the magnitude of the recovered anomaly is ~75% of the input anomaly. For both P- and S-wave data, the second test, with the assumed negative anomaly underneath the simplified structures, resolves the depth extent of the Kaapvaal cratonic keel with considerably less vertical smearing than test-a, while test-a better recovers amplitudes. As indicated, this third test (structure-driven assessment) is a more reliable way to check the vertical smearing effects (Allen and Tromp, 2005; Leveque and Masson, 1999; Alinaghi et al., 2007; Foulger et al., 2013).

Overall, the tests indicate that the vertical resolution of the thickness of the cratonic lithosphere is of the order of 100–200 km, as may be expected for teleseismic tomography where the energy is traveling subvertically. The horizontal resolution of the upper 200–300 km is ~100 km.

5. Results

The Kaapvaal and Zimbabwe cratonic keels have a prominent seismic high velocity anomaly (δVp and δVs range from 0.5 to 1.0% with respect to the reference model ak135) with low Vp/Vs ratio. The Kaapvaal Craton is imaged as a triangular high-velocity structure, which extends down to depths of 400–500 km. Taking the results of the resolution tests into account, this indicates that the lithospheric keel reaches depths of at least 300–350 km. Within the craton body, some small-scale features are imaged:

1) a noticeable contrast at the Colesberg Magnetic Lineament with ~0.6% in the S wave model, and a weak contrast in the P-wave model (Figs. 6, 7, Figs. S1, S2, S9),

2) the small northern block of Kaapvaal Craton (NKC) identified by an average positive anomaly of $\delta Vp = \sim 0.6\%$, between the negative anomalies of the eastern part of the Limpopo Belt and the Bushveld Complex (Figs. 6, 7), and

3) a continuous, relatively narrow, negative anomaly of $\delta Vs = \sim 0.5\%$ within the eastern block of the Kaapvaal Craton which extends from the apparent bottom of the keel. Apart from this narrow anomaly, no other differences between the eastern and western upper mantle domains of the Kaapvaal Craton are observed (Figs. 6, 7, Figs. S1, S9). To the west of the Kaapvaal Craton, the Kheis Belt is represented by a slightly negative velocity anomaly.

The Bushveld Complex appears as one unit with an average anomaly of ~0.5% in the P-wave model but vertical smearing impedes estimation of its depth extent (Fig. 5, Figs. S1, S6, S7). The Vp/Vs ratio is generally low (Fig. 6). The resolution tests indicate that the vertical resolution in this region is low, cf. the ~175–250 km smeared body attached to the real anomaly of the Bushveld Complex. The dense S-wave ray coverage shows a negative anomaly body with considerably less smearing than in the P-wave model. The S-wave model images separated negative anomalies for the eastern and western lobes of the Bushveld Complex (Figs. 6, 7, Figs. S1, S9). The present study indicates that the Bushveld Complex lobes may not be connected, thus supporting results for the crust from receiver functions analysis (Youssof et al., 2013). The estimated depth extent of the western lobe of Bushveld is ~150 km) shallows to the north to ~100 km, and it is undetermined beneath the eastern lobe.

The negative anomaly of $\delta Vp = \sim -0.75\%$ and $\delta Vs = \sim 0.60\%$ below the eastern block of the Limpopo Belt extends down to at least 250 km while a positive anomaly with $\delta Vp = \sim 0.60\%$ and $\delta Vs = \sim 0.50\%$ extends down to ~250 km below the western block (Fig. 7, S2, S3, S9). The vertical smearing, especially in the eastern

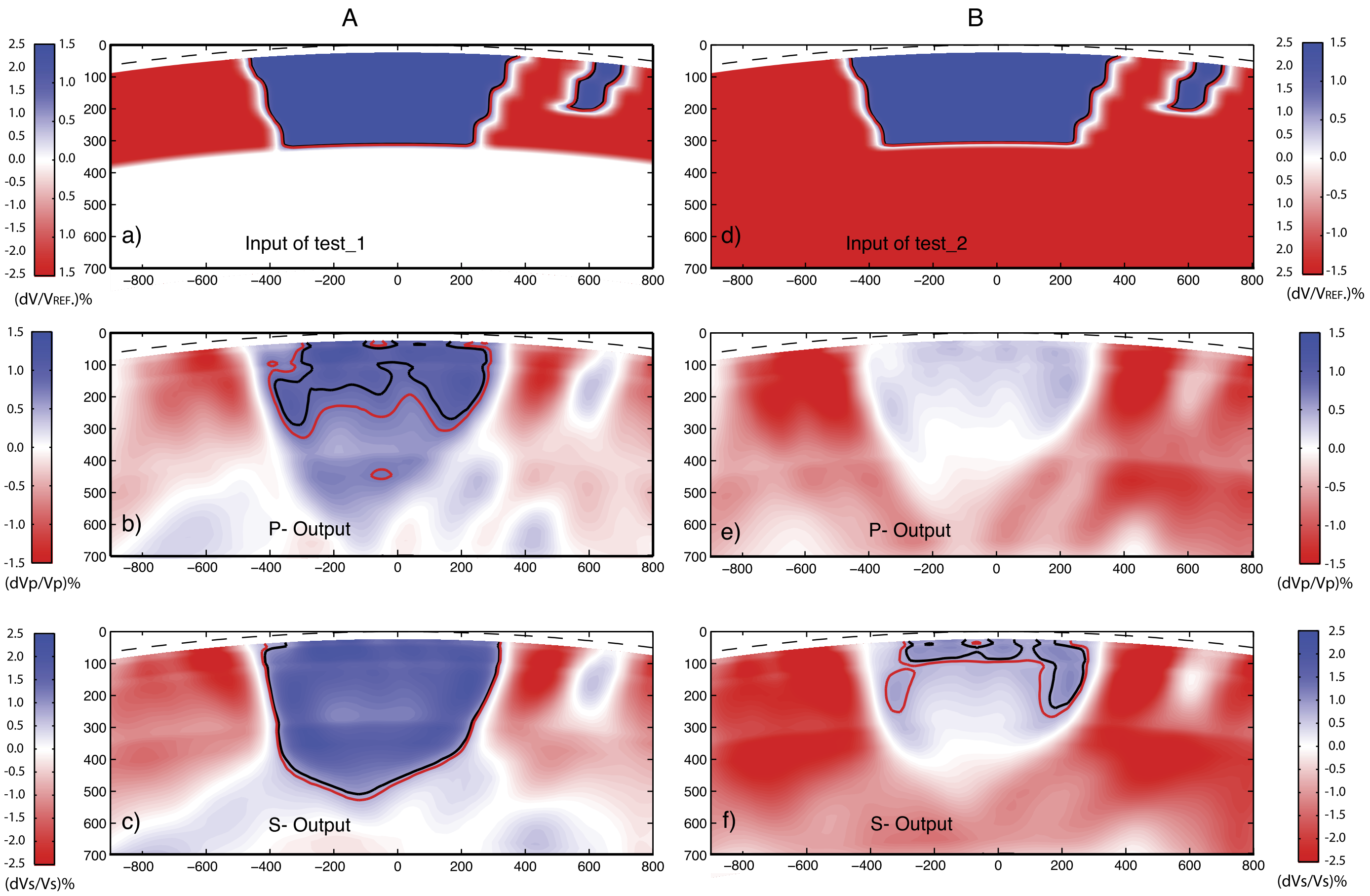

Fig. 5. Synthetic tests to examine the extent of vertical smearing in our model. Input models are shown on the upper panels (a, d) and recovered models are shown on panels b, e for P-wave and c, f for S-wave data. Left panels (A) are the structure-deriven test-1 which replicates the real P- and S-wave imaged anomalies where a) the input is underlained by zero anomaly, b) P-wave, and c) S-wave recovery results. Right panels (B) is the same as (A) but for the input of test 2, where the upper anomalie are underlained by a negative anomaly. (For interpretation of the colors in this figure, the reader is referred to the web version of this article.)

block, is significant and may reach ∼200 km, similar to the mantle anomaly below the Bushveld Complex. The southern collisional border between the Limpopo belt and the northern block of Kaapvaal Craton appears resolved (Figs. S2, S3). Although the Zimbabwe Craton is at the edge of the model with few seismic stations, both the P- and S-wave models include a ∼+1% anomaly in the southern Zimbabwe Cratonic area, which extends to a depth of ∼200 km (Fig. S1).

To the south of the Kaapvaal craton, we observe a ∼−0.5% negative anomaly which extends to at least a 200 km depth. A pronounced positive anomaly of ∼0.5% separates the Cape Fold and Namaqua–Natal mobile belts. This anomaly is observed below the tectonic surface expression of the collisional border of the two belts (Fig. 6).

6. Discussion

Our new 3D P- and S-wave tomography models present the expected first-order differences of the seismic velocity perturbations between the cratons, the modified cratons (such as the Bushveld complex) and the mobile belts, which surrounds the cratons (Fig. 6). The contrast in velocity perturbations between the cratons and the mobile belts is of the order of 1–2%, which is consistent with the anomalies expected from the compositional variations observed in mantle nodules (Shirey et al., 2003), although this number probably is underestimated due to smearing of the resulting velocity models. Compared to other previous seismic studies (e.g., Priestley et al., 2006; Fouch et al., 2004; Silver et al., 2001), our models are similar in most of the general aspects but they also show some significant differences.

Our results indicate the following features:

1. A pronounced positive anomaly is imaged below the northern part of the Kaapvaal Craton. It has a distinguishable contrast relative to the two surrounding blocks of the Limpopo Belt and the Bushveld Complex. Imaging such relatively small feature indicates better resolution by application of 3D Born sensitivity kernels than the previous ray theory-based studies of the area.
2. Our final images of the main Kaapvaal Craton indicate a different geometry of the lithospheric keel from what has been proposed earlier (Pearson, 1999). We observe a semi-triangular shape of the keel with a gentle slope of the cratonic edge to a depth of ∼300–350 km, whereas (Pearson, 1999) suggested a rectangular-like block with rough, steep edges to the surrounding belts. Our results indicate that the Kaapvaal cratonic keel extends to depths of 300–350 km (with an average velocity anomaly of ∼0.75%) and that the lithosphere beneath the southern Zimbabwe Craton is thinner (200–250 km) with an average velocity anomaly of ∼1%; the latter is imaged with lower resolution than the Kaapvaal Craton due to limited station coverage (Fig. 6, Fig. S1). Our estimated depth extent of the cratons agrees with James et al. (2001) who imaged a keel with ∼+1% anomaly to at least 300 km depth beneath the Kaapvaal Craton and to ∼250 km beneath the Zimbabwe Craton. Kaapvaal Craton is generally characterized by low Vp/Vs ratio (Fig. 6, Fig. S8) which may indicate a high magnesium

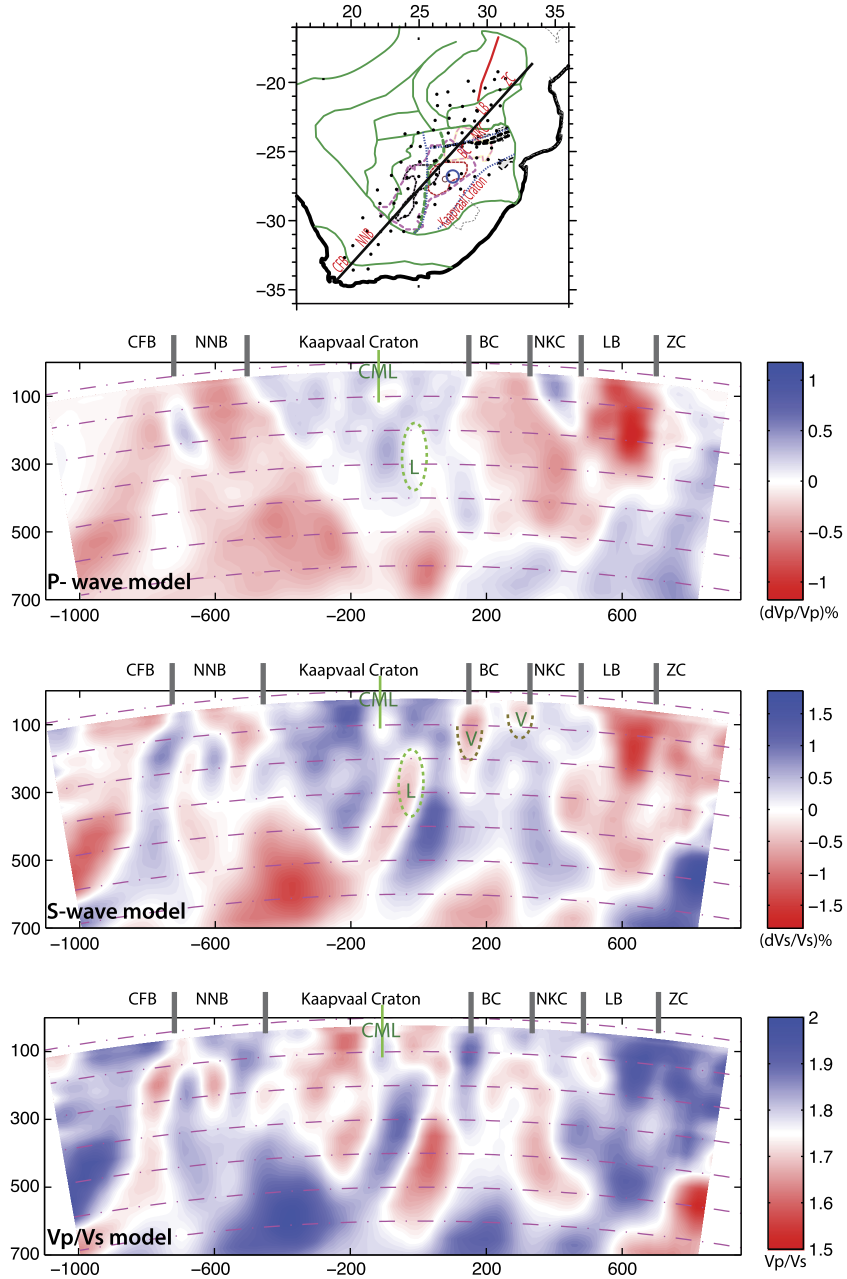

Fig. 6. Vertical sections for a) the P- and b) S-wave velocity from finite-frequency inversion of delay times corrected for elevation and crustal thickness. The vertical slices cut through the model along the selected NE–SW profile as indicated. This is a prefered profile and different from what shown in Fig. S1. c) Depth slice represents the Vp/Vs velocity model where the absolute ratio is calculated relative to ak135 as a reference model. Abbreviations: NKC: Northern block of the Kaapvaal Craton, CML: Colesberg Magnetic Lineament, ZC: Zimbabwe Craton, BC: Bushveld Complex, LB: Limpopo Belt, NNB: Namaqua–Natal Belt, and CFB: Cape Fold Belt. The dashed green ellipse shows the negative anomaly of ∼0.5% in the S-wave model within the eastern block of Kaapvaal Craton. The brown dashed lines represent the two lobes of the BC (marked by V) as in the S-wave model. The green dashed lines shown the thin low velocity zone within the Kaapvaal body (marked by L). (For interpretation of the references to color in this figure legend, the reader is referred to the web version of this article.)

number, i.e. a depleted composition (Lee, 2003). The presence of a depleted mantle below the cratonic crust may indicate that the crust and mantle have been connected since the formation of the craton.

3. The Colesberg Magnetic Lineament (CML), which may manifest subduction-related and collisional processes that occurred ∼2.7–2.9 Ga. Schmitz et al. (2004), is imaged with a contrast to the rest of the Kaapvaal Craton lithosphere. Profiles across the surface expression of the CML demonstrate this contrast (Figs. S1–S3). This new tomography imaged feature constrains the deep extent of the CML. This deep-reaching feature has also been confirmed by variations in Moho depth (Youssof et al., 2013) and in shallower crustal structure (de Wit and Tinker, 2004).
4. The ∼2.7 Ga Limpopo Belt between the Zimbabwe and Kaapvaal cratons is characterized by two different anomalies. The velocity anomaly of the eastern block has significantly larger amplitude (∼−0.75%) than proposed by James et al. (2001), Fouch et al. (2004) who estimate the magnitude of the anomaly to be ∼−0.5%. The seismic structure of the significant negative perturbations for that large part of the Limpopo Belt is unexpected but the associated anomaly (∼−0.75%) may be related to the Okavango Dyke Swarms. The seismic image of the western block of the Limpopo Belt shows

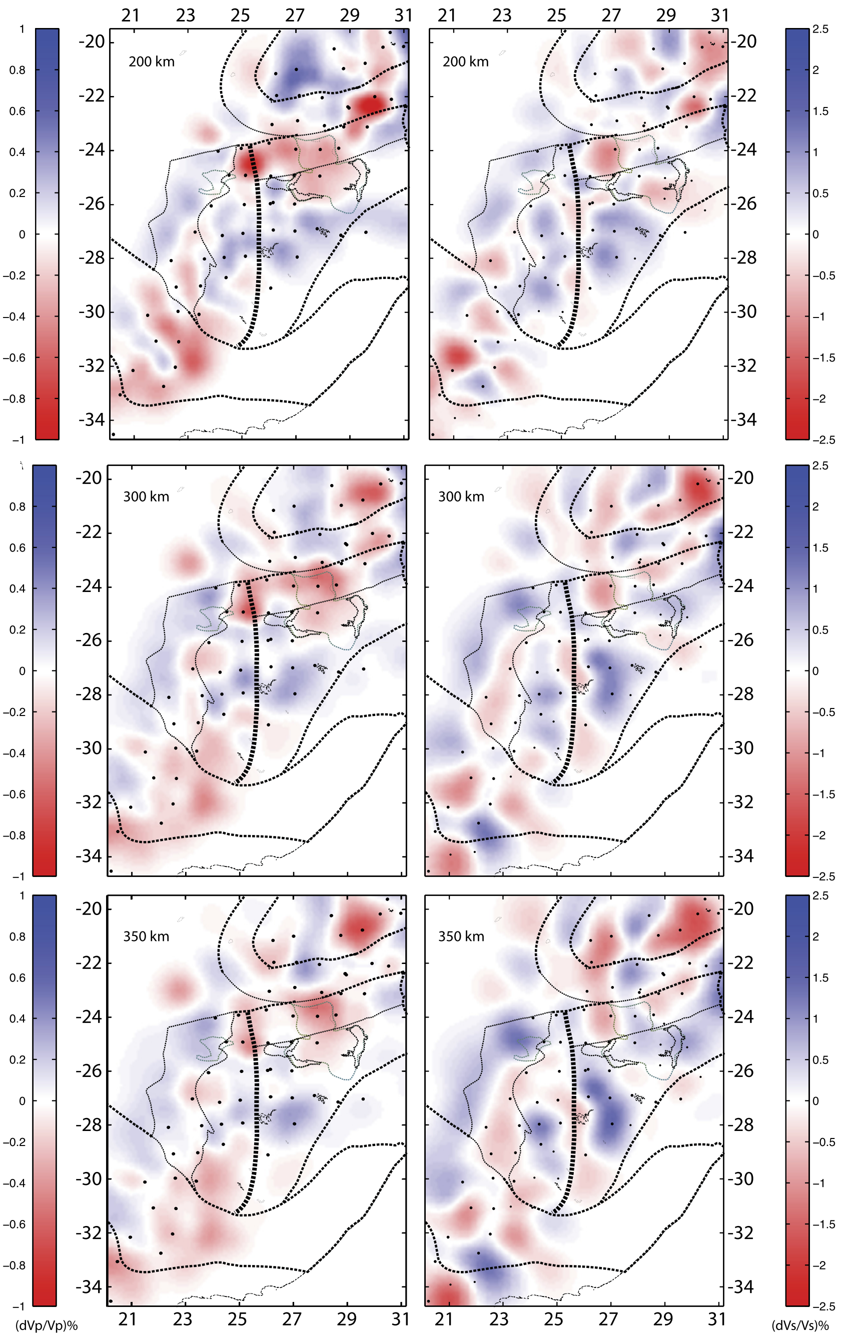

Fig. 7. Horizontal slices from of the models of P- and S-wave velocity perturbations at depths of 200, 300, and 350 km. (For interpretation of the colors in this figure, the reader is referred to the web version of this article.)

a positive anomaly of ∼0.75% which is in agreement with James et al. (2001), Fouch et al. (2004). For an interpretation for the mantle anomaly observed below the eastern Limpopo Belt, we note the following. a) Jordan (1979) reports that, in general, refertilized cratonic samples with significant weight percentage of clinopyroxene and garnet have seismic velocity decrease of 1% and density increase of 2–3% compared to depleted peridotites. Moreover, specifically for Limpopo, b) other studies (e.g., Watkeys and Armstrong, 1985; Zeh et al., 2007) suggest that fertilization processes involved an incompatible trace element-enriched fluid derived from dehydration of a slab, which subducted beneath the Limpopo region about 2.7 Ga, and c) the low velocity of the mantle in the Limpopo Belt may be caused by the existence of trapped fertilized peridotites, that may originate from underthrusting by oceanic and oceanic arc lithosphere (e.g., Lee, 2006; Snyder, 2008). And finally d) studies of other cratonic regions (e.g., the Slave Craton, Chen et al., 2009; Snyder et al., 2004, Siberia Griffin et al., 2005, and cratons globally Artemieva, 2009) do not exclude the involvement of metasomatic events that could fertilize the keel. Hence, we suggest that the Limpopo belt may include considerable amounts of impurities in the mantle with low seismic velocities, which can cause the observed anomalies. The source of these fertile patches within the depleted lithospheric mantle could originate from the collisional/accretionary processes at ∼2.7 Ga that amalgamated the present cratonic bodies and trapped fertile mantle in the suture zones between converging cratons.

5. Our model for the Bushveld Complex is in agreement with the model of James et al. (2001), Fouch et al. (2004) where the negative anomaly of $\sim -0.75\%$ extends down to a depth of $\sim$200 km (Figs. 6, 7). The presence of low *Vp*/*Vs* ratio indicates a depleted composition, thus supporting that the magma that formed the Bushveld complex originated from the mantle directly below the mafic intrusion. The Bushveld Complex represents a large igneous intrusive body (Von Gruenewaldt et al., 1985); it is generally accepted that its mantle has been chemically modified in the Proterozoic, ca. 2.05 Ga (Carlson et al., 2000), and that mantle refertilization significantly reduced the mantle velocity. Our S-wave model includes a positive anomaly in the area in-between the Bushveld lobes, where the ray coverage is dense. At crustal depths, recent receiver functions analysis and mapping of *Vp*/*Vs* (Youssof et al., 2013) also indicates that the mafic lobes are non-connected, in contrast to previous interpretation based on gravity anomalies (Webb et al., 2004, 2010).
6. The southern Cape Fold Belt and Namaqua–Natal Belt show average anomalies of $\sim -0.5\%$ but with a separation zone between them, below the surface exposure of the collision zone between the two belts at depth of $\sim$100 km. This image is in agreement with Lee (2006), James et al. (2001), especially for the P-wave tomography model.
7. The mobile belts, the Limpopo belt and the southern Zimbabwe Craton all are characterized by relatively high *Vp*/*Vs* ratio (Fig. 6, Fig. S8), which may indicate a more fertile composition than the Kaapvaal Craton.

Our resolution tests show that the lateral extent of the cratonic roots is reliably constrained (see Fig. 5, Figs. S6, S7). The effects of vertical smearing are roughly estimated using the integrated resolution tests, in particular, by the model-driven tests which shows that the smearing effects may extend dimensions by up-to 200 km vertically and not more than 50 km horizontally.

7. Conclusions

Teleseismic frequency-dependent tomography is used in the present study to image in high-resolution the upper mantle velocity structure of the cratons in southern Africa and the adjacent mobile belts. Using different resolution tests, we examined the range of the inherent smearing in the models. As it is well known, body wave tomography is much better for retrieving anomalies in the horizontal than vertical direction.

The results indicate that the depth extent of the fast lithospheric keel may be 300–350 km for the Kaapvaal Craton and 200–250 km for the southern part of the Zimbabwe Craton. The finite-frequency approach allows resolving relatively small-scale anomalies such as the lithosphere-scale suture zone between the eastern and western blocks of Kaapvaal Craton (the Colesberg Magnetic Lineament – (CML)) and the northern block of the Kaapvaal Craton. New tomographic images of the Bushveld Complex indicate that the surface exposures of its two lobes are non-connected in the mantle, similar to supporting finding in the crust by receiver function studies (Youssof et al., 2013).

The high resolution of the finite-frequency kernels makes it possible to recover the heterogeneous structure of the Limpopo Belt mantle. The mantle of the eastern Limpopo Belt has a negative velocity anomaly, comparable in magnitude to the mantle anomaly below the Bushveld Complex, where crossed by the Okavango Dyke Swarm. Our final tomographic images are in agreement with geochemical studies which indicates that fertilization processes changed the mantle of the Limpopo Belt during and after the collisional events between the Zimbabwe and Kaapvaal cratons (Meibom et al., 2003; Anderson, 2006).

Acknowledgements

This project received financial support through grants FNU11-104254, DFF-1323-00053 and FNU10-83081 from the Danish Natural Research Council. The authors thank Brandon Schmandt, Eugene Humphreys and Max Bezada of the University of Oregon for providing the finite-frequency tomography codes used in this study. Max Bezada (now at University of Minnesota) was very helpful with giving instructions on the use of the MATLAB codes used in this study. The authors are grateful to Peter Shearer and two anonymous reviewers for the constructive comments, which enhanced the quality of the paper.

Appendix A. Supplementary material

Printable figures (grayscale and modified color) and supplementary material related to this article can be found online at http://dx.doi.org/10.1016/j.epsl.2015.01.034.

References

Abt, D., Fischer, K., French, S., Ford, H., Yuan, H., Romanowicz, B., 2010. North American lithospheric discontinuity structure imaged by Ps and Sp receiver functions. J. Geophys. Res. 115. http://dx.doi.org/10.1029/2009JB006914.

Adams, A., Nyblade, A., 2011. Shear wave velocity structure of the southern African upper mantle with implications for the uplift of southern Africa. Geophys. J. Int. 186, 808–824.

Alinaghi, A., Koulakov, I., Thybo, H., 2007. Seismic tomographic imaging of P- and S-waves velocity perturbations in the upper mantle beneath Iran. Geophys. J. Int. 169 (3), 1089–1102. http://dx.doi.org/10.1111/j.1365-246X.2007.03317.x.

Allen, R.M., Tromp, J., 2005. Resolution of regional seismic models: squeezing the Iceland anomaly. Geophys. J. Int. 161, 373–386.

Anderson, D., 2006. Speculations on the nature and cause of mantle heterogeneity. Tectonophysics 416, 7–22.

Artemieva, I.M., 2009. The continental lithosphere: reconciling thermal, seismic, and petrologic data. Lithos 109, 23–46.

Artemieva, I.M., 2011. The Lithosphere: An Interdisciplinary Approach. Cambridge Univ. Press, 794 pp.

Artemieva, I.M., Mooney, W.D., 2001. Thermal thickness and evolution of Precambrian lithosphere; a global study. J. Geophys. Res. 106, 16387–16414.

Bezada, M.J., Levander, A., Schmandt, B., 2010. Subduction in the southern Caribbean: images from finite-frequency P wave tomography. J. Geophys. Res. 115, B12333. http://dx.doi.org/10.1029/2010JB007682.

Boyd, F.R., 1987. High- and low-temperature garnet peridotite xenoliths and their possible relation to the lithosphere–asthenosphere boundary beneath southern Africa. In: Nixon, P.H. (Ed.), Mantle Xenoliths. John Wiley, New York, pp. 403–412.

Boyd, F.R., Pearson, D.G., Nixon, P.H., Mertzman, S.A., 1993. Low-calcium garnet harzburgites from southern Africa – their relations to craton structure and diamond crystallization. Contrib. Mineral. Petrol. 113, 352–366.

Carlson, R.W., Boyd, F.R., Shirey, S.B., Janney, P.E., Grove, T.L., Bowring, S.A., Schmitz, M.D., Dann, J.C., Bell, D.R., Gurney, J.J., Richardson, S.H., Tredoux, M., Menzies, A.H., Pearson, D.G., Hart, R.J., Wilson, A.H., Moser, D., 2000. Continental growth, preservation and modification in southern Africa. GSA Today 10, 1–7.

Carlson, R.W., Grove, T.L., de Wit, M.J., Gurney, J.J., 1996. Anatomy of an Archean craton: a program for interdisciplinary studies of the Kaapvaal craton, southern Africa. Eos Trans. AGU 77, 273–277.

Chen, C.-W., Rondenay, S., Evans, R.L., Snyder, D.B., 2009. Geophysical detection of relict metasomatism from an Archean ($\sim$3.5 Ga) subduction zone. Science 326, 1089–1091.

Chevrot, S., Zhao, L., 2007. Multiscale seismic tomography finite-frequency Rayleigh wave tomography of the Kaapvaal craton. Geophys. J. Int. 169, 201–215.

Cooper, C.M., Miller, M.S., 2014. Craton formation: internal structure inherited from closing of the early oceans. Lithosphere 6, 35–42. http://dx.doi.org/10.1130/L321.1.

Dahlen, F.A., Hung, S.H., Nolet, G., 2000. Fréchet kernels for finite-frequency traveltimes—I. Theory. Geophys. J. Int. 141, 157–174.

Darbyshire, F., et al., 2012. Seismic imaging of the lithosphere beneath Hudson Bay: episodic growth of the Laurentian mantle keel. Earth Planet. Sci. Lett. 373, 179–193. http://dx.doi.org/10.1016/j.epsl.2013.05.002.

de Hoop, M., van der Hilst, R., 2005. On sensitivity kernels for 'wave-equation' transmission tomography. Geophys. J. Int. 160, 621–633.

de Wit, M.J., Tinker, J., 2004. Crustal structures across the central Kaapvaal Craton from deep-seismic reflection data. S. Afr. J. Geol. 107, 185–206.

Eaton, D., et al., 2009. The elusive lithosphere–asthenosphere boundary (LAB) beneath cratons. Lithos 109 (1–2), 1–22. http://dx.doi.org/10.1016/j.lithos.2008.05.009.

Eberhart-Philips, D., 1986. Three-dimensional velocity structure in northern California coast ranges from inversion of local earthquakes. Bull. Seismol. Soc. Am. 76, 1025–1052.

Finnerty, A.A., Boyd, J.J., 1987. Thermobarometry for garnet peridotites: basis for the determination of thermal and compositional structure of the upper mantle. In: Nixon, P.H. (Ed.), Mantle Xenoliths. John Wiley, New York, pp. 381–402.

Fischer, K.M., Ford, H.A., Abt, D.L., Rychert, C.A., 2010. The lithosphere–asthenosphere boundary. Annu. Rev. Earth Planet. Sci. 38, 551–575.

Fishwick, S., Kennett, B., Reading, A., 2005. Contrasts in lithospheric structure within the Australian craton—insights from surface wave tomography. Earth Planet. Sci. Lett. 231, 163–176.

Fouch, M.J., James, D.E., VanDecar, J.C., van der Lee, S., The Kaapvaal Seismic Group, 2004. Mantle seismic structure beneath the Kaapvaal and Zimbabwe cratons. S. Afr. J. Geol. 107, 35–46.

Foulger, et al., 2013. Caveats on tomographic images. Terra Nova 25, 259–281.

Griffin, W.L., Natapov, L.M., O'Reilly, S.Y., van Achterbergh, S.Y., Cherenkova, A.F., Cherenkov, V.G., 2005. The Kharamai kimberlite field, Siberia: modification of the lithospheric mantle by the Siberian Trap event. Lithos (ISSN 0024-4937) 81, 167–187. http://dx.doi.org/10.1016/j.lithos.2004.10.001.

Gung, Y., Panning, M.P., Romanowicz, B., 2003. Global anisotropy and the thickness of continents. Nature 422, 707–711.

Hansen, S., Nyblade, A., Julia, J., Dirks, P., Durrheim, R., 2009. Upper-mantle low-velocity zone structure beneath the Kaapvaal craton from S-wave receiver functions. Geophys. J. Int. 178, 1021–1027.

Hopper, E., Ford, H.A., Fischer, K.M., Lekic, V., Fouch, M.J., 2014. The lithosphere–asthenosphere boundary and the tectonic and magmatic history of the northwestern United States. Earth Planet. Sci. Lett.. http://dx.doi.org/10.1016/j.epsl.2013.12.016.

Hung, S.-H., Dahlen, F.A., Nolet, G., 2000. Fréchet kernels for finite-frequency traveltimes: II. Examples. Geophys. J. Int. 141, 175–203.

James, D., Fouch, M.J., VanDecar, J.C., Van der Lee, S., The Kaapvaal Seismic Group, 2001. Tectospheric structure beneath southern Africa. Geophys. Res. Lett. 28 (13), 2485–2488.

Jordan, T.H., 1975. The continental tectosphere. Rev. Geophys. 13, 1–12.

Jordan, T.H., 1978. Composition and development of the continental tectosphere. Nature 274, 544–548.

Jordan, T.H., 1979. Mineralogies, densities and seismic velocities of garnet lherzolites and their geophysical implications. In: Boyd, F.R., Meyer, H.O.A. (Eds.), The Mantle Sample: Inclusions in Kimberlites and Other Volcanics. Am. Geophys. Union, Washington, D.C., United States, pp. 1–14.

Jordan, T.H., 1988. Structure and formation of the continental tectosphere. In: Menzies, M.A., Cox, K.G. (Eds.), J. Petrology (Special Lithosphere Issue), 11–37. Trans. R. Soc. London, London, United Kingdom.

Kennett, B.L.N., Engdahl, E.R., Buland, R., 1995. Constraints on seismic velocities in the Earth from travel times. Geophys. J. Int. 122, 108–124.

Kopylova, M.G., McCammon, 2003. Composition and the redox state of the Slave peridotitic mantle. In: Proc. 8th Intern. Kimberlite Conf. Victoria, BC, Canada, June 2003, FLA-0195.

Kopylova, M.G., Russell, J.K., 2000. Chemical stratification of cratonic lithosphere: constraints from the northern Slave craton, Canada. Earth Planet. Sci. Lett. 181, 71–87.

Kumar, P., et al., 2007. The rapid drift of the Indian tectonic plate. Nature 449, 894–897.

Lebedev, S., Boonen, J., Trampert, J., 2009. Seismic structure of Precambrian lithosphere: new constraints from broad-band surface-wave dispersion. Lithosphere 109, 96–111. http://dx.doi.org/10.1016/j.lithos.2008.06.010.

Lee, C.-T.A., 2006. Geochemical/petrologic constraints on the origin of cratonic mantle. In: Benn, K., Mareschal, J.-C., Condie, K.C. (Eds.), Archean Geodynamics and Environments. In: Am. Geophys. Union Monogr., vol. 164, pp. 89–114.

Lee, C.-T.A., 2003. Compositional variation of density and seismic velocities in natural peridotites at STP conditions: implications for seismic imaging of compositional heterogeneities in the upper mantle. J. Geophys. Res. 108 (B9), 2441. http://dx.doi.org/10.1029/2003JB002413.

Lehtonen, M., O'Brien, H.E., Peltonen, P., Johanson, B.S., Pakkanen, L., 2004. Layered mantle at the Karelian Craton margin: P–T of mantle xenocrysts and xenoliths from the Kaavi–Kuopio kimberlites, Finland. Lithos 77, 593–608.

Lekić, V., Fischer, K.M., 2013. Contrasting lithospheric signatures across the western United States revealed by Sp receiver functions. Earth Planet. Sci. Lett.. http://dx.doi.org/10.1016/j.epsl.2013.11.026.

Lerner-Lam, A.L., Jordan, T.H., 1987. How thick are the continents? J. Geophys. Res. 92, 14007–14026.

Levander, et al., 2006. Imag(in)ing the continental lithosphere. Tectonophysics (ISSN 0040-1951) 416, 167–185. http://dx.doi.org/10.1016/j.tecto.2005.11.018.

Leveque, J., Masson, F., 1999. From ACH tomographic models to absolute velocity models. Geophys. J. Int. 137, 621–629.

Li, A., Burke, K., 2006. Upper mantle structure of southern Africa from Rayleigh wave tomography. J. Geophys. Res. 111. http://dx.doi.org/10.1029/2006JB004321.

Marquering, H., Dahlen, F.A., Nolet, G., 1999. Three dimensional sensitivity kernels for finite-frequency traveltimes: the banana-doughnut paradox. Geophys. J. Int. 137, 805–815.

Meibom, A., Anderson, D.L., Sleep, N.H., Frei, R., Chamberlain, C.P., Hren, M.T., Wooden, J.L., 2003. Are high ^{3}He/^{4}He ratios in oceanic basalts an indicator of deep-mantle plume components? Earth Planet. Sci. Lett. 208, 197–204.

Montelli, R., Nolet, G., Masters, G., Dahlen, F.A., Hung, S.-H., 2004a. Global P and PP traveltime tomography: rays versus waves. Geophys. J. Int. 158, 637–654.

Montelli, R., Nolet, G., Dahlen, F.A., Masters, G., Engdahl, E.R., Hung, S.-H., 2004b. Finite frequency tomography reveals a variety of plumes in the mantle. Science 303, 338–343.

Paige, C.C., Saunders, M.A., 1982. LSQR: an algorithm for sparse, linear equations and sparse least squares. ACM Trans. Math. Softw. 8, 43–71.

Pearson, D.G., 1999. The age of continental roots. Lithos 48, 171–194.

Pearson, D.G., Carlson, R.W., Shirey, S.B., Boyd, F.R., Nixon, P.H., 1995. Stabilisation of Archaean lithospheric mantle: a Re–Os isotope study of peridotite xenoliths from the Kaapvaal craton. Earth Planet. Sci. Lett. 134, 341–357.

Perchuć, E., Thybo, H., 1996. A new model of upper mantle P-wave velocity below the Baltic Shield: indication of partial melt in the 95 to 160 km depth range. Tectonophysics (ISSN 0040-1951) 253 (3–4), 227–245. http://dx.doi.org/10.1016/0040-1951(95)00057-7.

Priestley, K., McKenzie, D., Debayle, E., 2006. The state of the upper mantle beneath Southern Africa. Tectonophysics 416, 101–112.

Priestley, K., et al., 2008. The African upper mantle and its relationship to tectonics and surface geology. Geophys. J. Int. 175 (3), 1108–1126.

Priestley, K., Tilmann, F., 2009. Relationship between the upper mantle high velocity seismic lid and the continental lithosphere. Lithos 109, 112–124.

Ritsema, J., Van Heijst, H.J., Woodhouse, J.H., Deuss, A., 2009. Long-period body wave traveltimes through the crust: implication for crustal corrections and seismic tomography. Geophys. J. Int. 179 (2), 1255–1261. http://dx.doi.org/10.1111/j.1365-246X.2009.04365.x.

Rudnick, L.R., McDonough, W.F., O'Connell, R.J., 1998. Thermal structure, thickness and composition of continental lithosphere. Chem. Geol. 145, 395–411.

Rychert, C., Shearer, P., 2009. A global view of the lithosphere–asthenosphere boundary. Science 324, 495–498. http://dx.doi.org/10.1126/science.1169754.

Schmandt, B., Humphreys, E., 2010. Seismic heterogeneity and small-scale convection in the southern California upper mantle. Geochem. Geophys. Geosyst. 11, Q05004.

Schmitz, M.D., Bowring, S.A., de Wit, M.J., Gartz, V., 2004. Subduction and terrane collision stabilized the western Kaapvaal craton tectosphere 2.9 billion years ago. Earth Planet. Sci. Lett. 222, 363–376.

Sebai, A., Stutzmann, E., Montagner, J.P., Sicilia, D., Beucler, E., 2006. Anisotropic structure of the African upper mantle from Rayleigh and Love tomography. Phys. Earth Planet. Inter. 155, 48–62.

Shirey, S.B., et al., 2003. Regional patterns in the paragenesis and age of inclusions in diamond, diamond composition, and the lithospheric seismic structure of Southern Africa. Lithos 71, 243–258.

Shirey, S.B., Harris, J.W., Richardson, S.R., Fouch, M.J., James, D.E., Cartigny, P., Deines, P., Viljoen, F., 2002. Diamond genesis, seismic structure, and evolution of the Kaapvaal–Zimbabwe craton. Science 297, 1683–1686.

Shirey, S.B., Richardson, S.H., Menzies, A.H., Pearson, D.G., Harris, J.W., Carlson, R.W., Wiechert, U., Gurney, J.J., 2001. Emplacement of eclogite components into the lithospheric mantle during craton formation. Geophys. Res. Lett. 28, 2509–2512.

Silver, P.G., Gao, S.S., Liu, K.H., The Kaapvaal Seismic Group, 2001. Mantle deformation beneath southern Africa. Geophys. Res. Lett. 28, 2493–2496.

Snyder, D.B., 2008. Stacked uppermost mantle layers within the Slave craton of NW Canada as defined by anisotropic seismic discontinuities. Tectonics 27, TC4006. http://dx.doi.org/10.1029/2007TC002132.

Snyder, D.B., Rondenay, S., Bostock, M.G., Lockhart, G.D., 2004. Mapping the mantle lithosphere for diamond potential using teleseismic methods. Lithos 77, 859–872.

Sodoudi, F., et al., 2014. Seismic evidence for stratification in composition and anisotropic fabric within the thick lithosphere of Kalahari Craton. Geochem. Geophys. Geosyst. 14, 5393–5412. http://dx.doi.org/10.1002/2013GC004955.

Thybo, H., Perchuć, E., 1997. The seismic 8 degrees discontinuity and partial melting in continental mantle. Science 275, 1626–1629.

Thybo, H., 2006. The heterogeneous Upper Mantle Low Velocity Zone. Tectonophysics 416, 53–79.

VanDecar, J.C., Crosson, R.S., 1990. Determination of teleseismic relative phase arrival times using multi-channel cross correlation and least squares. Bull. Seismol. Soc. Am. 80, 150–159.

Vinnik, L.P., Green, R.W.E., Nicolaysen, L.O., Kosarev, G.L., Petersen, N.V., 1996. Deep seismic structure of the Kaapvaal Craton. Tectonophysics 262, 67–75.

Vinnik, L., et al., 2009. Mantle anomalies beneath southern Africa: evidence from seismic S and P receiver functions. Geophys. J. Int., 279–298.

Von Gruenewaldt, G., Sharpe, M.R., Hatton, C.J., 1985. The Bushveld Complex: introduction and review. Econ. Geol. 80, 803–812.

Watkeys, M.K., Armstrong, R.A., 1985. The importance of being Alkaline-deformed late Archaean lamprophyric dykes, Central Zone, Limpopo belt. Trans. Geol. Soc. S. Afr. 88, 195–206.

Webb, S.J., Ashwal, L.D., Cawthorn, R.G., 2010. Continuity between eastern and western Bushveld Complex, South Africa, confirmed by xenoliths from kimberlite. Contrib. Mineral. Petrol. 162, 101–107. http://dx.doi.org/10.1007/s00410-010-0586-z.

Webb, S.J., Cawthorn, R.G., Nguuri, T.K., James, D.E., 2004. Gravity modeling of Bushveld Complex connectivity supported by Southern African seismic experiment results. S. Afr. J. Geol. 107, 207–218.

Wirth, E.A., Long, M.D., 2014. A contrast in anisotropy across mid-lithospheric discontinuities beneath the central United States – a relic of craton formation. Geology 42, 851–854.

Wittlinger, G., Farra, V., 2007. Converted waves reveal a thick and layered tectosphere beneath the Kalahari super-craton. Earth Planet. Sci. Lett. 254, 404–415.

Youssof, M., Thybo, H., Artemieva, I.M., Levander, A., 2013. Moho depth and crustal composition in the Southern Africa. Tectonophysics. http://dx.doi.org/10.1016/j.tecto.2013.09.001.

Yuan, H., Romanowicz, B., 2010. Lithospheric layering in the North American craton. Nature 466, 1063–1168.

Zeh, A., Gerdes, A., Klemd, R., Barton, J.M. Jr, 2007. Archaean to Proterozoic crustal evolution in the central zone of the Limpopo Belt (South Africa–Botswana): constraints from combined U–Pb and Lu–Hf isotope analyses of zircon. J. Petrology 48 (8), 1605–1639. http://dx.doi.org/10.1093/petrology/egm032.

Zhao, M., Langston, C., Nyblade, A., Owens, T., 1999. Upper mantle velocity structure beneath southern Africa from modeling regional seismic data. J. Geophys. Res. 104, 4783–4794.